

# Retro-Reflective Beam Communications with Spatially Separated Laser Resonator

Mingliang Xiong, Mingqing Liu, Qingwei Jiang, Jie Zhou, Qingwen Liu\*, *Senior Member, IEEE*, and Hao Deng

## Abstract

Optical wireless communications (OWC) which utilizes infrared or visible light as the carrier attracts great attention in 6G research. Resonant beam communications (RBCom) is an OWC technology which simultaneously satisfies the needs of non-mechanical mobility and high signal-to-noise ratio (SNR). It has the self-alignment feature and therefore avoids positioning and pointing operations. However, RBCom undergoes echo interference. In this paper, we propose an echo-interference-free RBCom system design based on second harmonic generation. The transmitter and the receiver constitute a spatially separated laser resonator, in which the retro-reflective resonant beam is formed and tracks the receiver automatically. This structure provides a channel with adaptive capability in beamforming and alignment, which is similar to the concept of intelligent reflecting surface (IRS) enhanced communications, but without hardware and software controllers. Besides, we establish an analytical model to evaluate the beam radius, the beam power, and the channel capacity. The results show that our system achieves longer distance and smaller beam diameter for the transmission beyond 10 Gbit/s, compared with the existing OWC technologies.

## Index Terms

Optical wireless communications, resonant beam communications, laser communications, second harmonic generation, 6G mobile communications.

## I. INTRODUCTION

The ever-ending pursuit of higher data rate sets the goal for the next-decade wireless services: providing at least a challenging Tb/s-level bit rate. A key advancement in 6G is changing the way of indoor communications, from radio-frequency (RF) communications to free-space optical communications (FSO) [1]. Since the light frequency lies in the range of several hundred THz, which means very large bandwidth can be obtained, FSO has the potential to support Tbit/s-level data transmission.

Existing FSO technologies include non-directional light (e.g., LED radiation) and directional light (e.g., laser beam). As shown in Fig. 1(a), the light from the LED base station (BS) is emitted at a large angle. Mobile stations (MSs) within the coverage area can receive the light signal from the BS. However, the received light intensity decreases quickly as the distance grows. In a nutshell, non-directional light supports high mobility and

\* The corresponding author: Qingwen Liu.

M. Xiong, M. Liu, Q. Jiang, J. Zhou, Q. Liu, and H. Deng are with the College of Electronics and Information Engineering, Tongji University, Shanghai 201804, China (xiongml@tongji.edu.cn; clare@tongji.edu.cn; jiangqw@tongji.edu.cn; jzhou@tongji.edu.cn; qliu@tongji.edu.cn; and denghao1984@tongji.edu.cn).

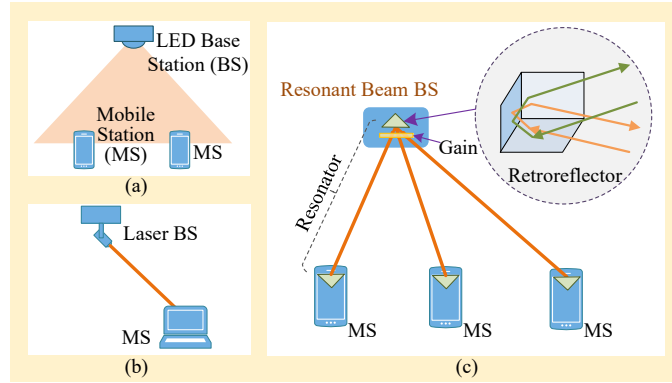


Fig. 1: Comparison of communication technologies with: (a) non-directional radiation; (b) directional radiation; (c) retro-reflective resonant beam

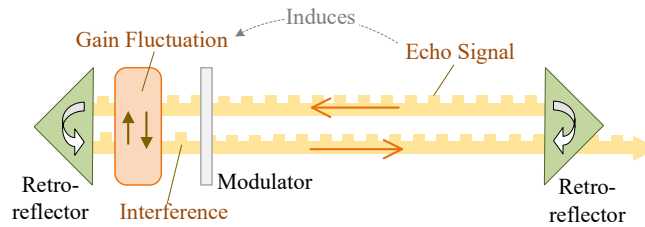


Fig. 2: Echo interference issue in resonant beam communications system

multiple accessing but undergoes remarkable path loss [2]. In contrast, directional light has higher power density and smaller path loss than non-directional light, as shown in Fig. 1(b). However, directional light needs positioning and beam steering to implement alignment and tracking of MSs, which highly demands response speed and accuracy [3]. Generally, fiber array can be used as the light source to generate directional beams; this design has achieved data rate of 10 Gbit/s [4]. Through tilted fiber grating, light beam carrying 12 Gbit/s data can be directed to the receiver at different location [5]. Spatial light modulator (SLM) can be employed to generate hologram which is able to be controlled to cover specific receivers [6]. Rhee *et al.* employed optical phase array (OPA) to generate beams to arbitrary direction, and achieved the data rate of 32 Gbit/s [7]. Chun *et al.* used micro-electro-mechanical system (MEMS) mirror to steer the light beam, and achieved the data rate of 35 Gbit/s [8]. However, these technologies require positioning technology to acquire the accurate location of the receiver, which increases the costs and complexity. Besides, the mobility of these technologies is limited by the transmission delay of positioning signal, the refresh frequency of OPA, or the response speed MEMS.

Figure 1(c) depicts the resonant beam communications (RBCom) system, in which both the BS and the MS contain a retroreflector to reflect the incident lights back along the incident direction. Similar to the intelligent reflecting surface (IRS) enhanced communication which adjusts the channel state to improve the performance, RBCom channel has the adaptive ability in beamforming and alignment [9]. Two retroreflectors form a spatially distributed laser resonator naturally without the need of strict alignment, providing RBCom with self-alignment

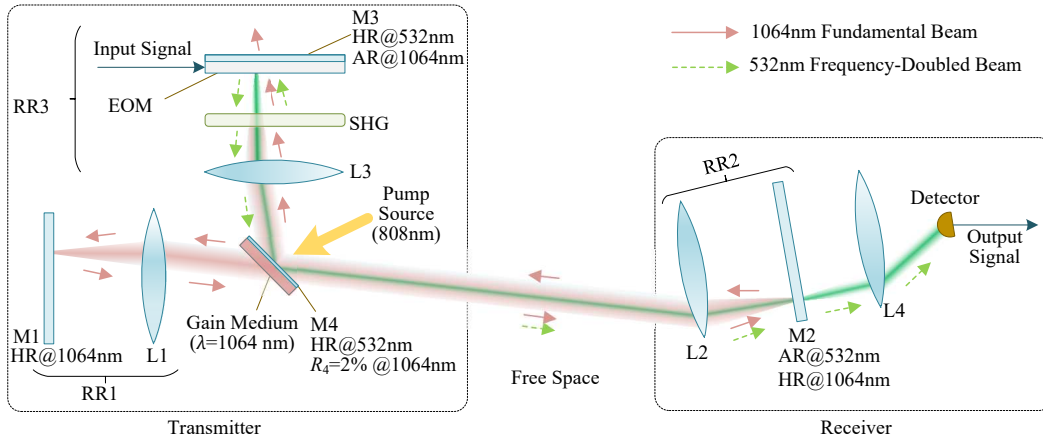


Fig. 3: Echo-interference-free design for resonant beam communications system with second harmonic generation (AR: anti-reflective coating, i.e., 100% transmissivity; HR: high-reflective coating, i.e., 100% reflectivity; L1, L2, L3, and L4 are lenses; M1, M2, M3, and M4 are flat mirrors; RR1, RR2, and RR3 are retroreflectors; EOM: electro-optical modulator; SHG: second harmonic generation medium;  $R_4$ : reflectivity of M4 at 1064 nm)

feature and mobility [10–12]. In this retro-reflective resonator, photons generated by the gain medium through spontaneous emission; then, they travel back and forth and are enhanced by superposition. In this case, an intra-cavity resonant beam is spontaneously formed, connecting the BS and the MS. The source power drives the gain medium to provide a power amplification capability. As the transmission loss is compensated by the gain, the beam power can reach a considerable level to support high SNR [13, 14].

However, the RBCom system undergoes echo interference. As in Fig. 2, the transmitted signal is reflected back to the transmitter’s gain medium and modulator by the receiver’s retroreflector, affecting the gain stability and the subsequent modulation. This characteristic plus its solution relying on frequency-band shifting and optical filtering are presented in [15, 16]. Nevertheless, even narrow-band optical filters are used, the modulator still has to operate at tens of GHz to ensure that the signal frequency lies out of the filter’s passband. As high-speed modulation is supported by splitting the modulator’s surface into small pixels, the driving power as well as the temperature will increase to a prohibitive level [17]. The demands for a practical and economic echo-interference-free RBCom systems motivate this work.

In this paper, to avoid echo interference, we exploit the fact that only the light wave in a certain frequency band affects the stimulation emission of the gain medium, and thus design a coupled optical path with second harmonic generation (SHG) to produce frequency-doubled carrier beam which lies out of the gain medium’s stimulation frequency band. At the transmitter, the fundamental beam for SHG is extracted from the resonant beam formed within the spatially separated resonator through a coated mirror M4. At the receiver, the frequency-doubled beam passes through a partially reflective mirror M2 to the detector, while the low-frequency resonant beam is reflected to maintain the resonance. The coupled design allows the frequency-doubled beam transmitting along the free-space path of the resonant beam which automatically keeps pointing to the receiver at any time. The modulator only

changes the frequency-doubled beam, so the resonant beam remains stable, avoiding echo interference.

The contributions of this work are as follows.

- 1) We propose an SHG-based RCom system design, which solves the echo interference problem of the original RCom system, providing non-mechanical mobility and high capacity.
- 2) We establish an analytical model for the SHG-based RCom system which can evaluate the beam radius, diffraction loss, beam power, and channel capacity, without the need of a numerical computing program that is usually adopted for evaluating such multi-lens resonator.

The remainder of this paper is organized as follows. Section II details the model of the self-interference-free RCom system. Section III presents the performance evaluation of the proposed model. Section IV discusses several issues for further research. Finally, conclusions are drawn in Section V.

## II. SYSTEM MODEL

### A. System Design

The SHG-based RCom system consists of two coupled parts, i.e., the spatially separated laser resonator and the SHG path. A portion of the fundamental beam generated by the resonator is coupled into the SHG path and is converted into a frequency-doubled beam which serves as the communication carrier. After modulation, the frequency-doubled beam is coupled into the original fundamental beam path, and propagates to the receiver along this path.

As depicted in Fig. 3, RR1 and RR2 are retroreflectors with cat's eye structure, and are installed in the transmitter and the receiver, respectively. The spatially separated laser resonator is constituted by RR1, the gain medium, and RR2. The gain medium absorbs pump source light to enable optical amplification. Here Nd:YVO<sub>4</sub> crystal is employed as the gain medium, hence, the pump source is 808-nm light (usually generated by laser diodes; in addition to 808 nm, some other wavelengths such as 880 nm can also be used for pumping the Nd:YVO<sub>4</sub> crystal), and 1064-nm light can be amplified. According to the mechanism of laser resonators, 1064-nm resonant beam can be generated in this resonator.

The surface on one side of the gain medium has a thin coating M4 which can reflect all the 532-nm beam and a portion (e.g., reflectivity  $R_4 = 2\%$ ) of 1064-nm beam. Hence, the 1064-nm resonant beam in the resonator is split by the partially reflective surface M4; a portion of the resonant beam is extracted as the fundamental beam for SHG; and the rest still stays in the resonating path between RR1 and RR2 to maintain the resonance. The 1064-nm fundamental beam enters the retroreflector RR3 and passes the SHG medium to generate 532-nm frequency-doubled beam.

The 532-nm beam is modulated by the electro-optical modulator (EOM) and then reflected by mirror M3. Since RR1 and RR3 are designed to be mirror symmetric about M4, and they have capability of retro-reflection, the modulated 532-nm beam can travel along the original path of the incident 1064-nm beam. After being reflected by M4, the modulated 532-nm beam is coupled into the free-space propagating path of the resonant beam and received by the receiver. Mirror M2 is coated to reflect only 1064-nm beam. Thus, the 532-nm beam can pass through M2. Finally, the 532-nm beam is focused on the photon detector (PD) by lens L4.

In RBCom, the modulated signals can pass through the mirror M2, without interference on the gain and the modulation operation. The fundamental beam is retro-reflected by M2 to maintain the resonance, which provides an automatically tracking path towards the receiver.

### B. Telecentric Cat's Eye Retroreflector

There are several kinds of retroreflectors, such as corner cube, cat's eye, and telecentric cat's eye, to constitute spatially separated laser resonators and enable the self-alignment features. In this work, we exploit the telecentric cat's eye retroreflector, since it has the following unique optical characteristics. As depicted in Fig. 4, the telecentric cat's eye consists of a flat rear mirror whose radius of curvature (ROC) is infinite and a lens whose focal length is  $f$ . The interval between the mirror and the lens is  $l$ . A pupil locates at the right focal point of the lens. The light beam entering the pupil from arbitrary directions will: 1) be perpendicular to the rear mirror after passing through the lens; and 2) exit through the pupil along the original path of the incident beam.

Ray-transfer matrices are adopted to describe an optical system under the paraxial approximation. All the optical elements and the free spaces in the system are represented by individual matrices. The system ray-transfer matrix is the production of these individual matrices with the opposite order [18]. For the cat's eye shown in Fig. 5, the matrix is

$$\begin{aligned} \mathbf{M}_{\text{RR}} &= \begin{bmatrix} 1 & f \\ 0 & 1 \end{bmatrix} \begin{bmatrix} 1 & 0 \\ -1/f & 1 \end{bmatrix} \begin{bmatrix} 1 & l \\ 0 & 1 \end{bmatrix} \begin{bmatrix} 1 & 0 \\ 0 & 1 \end{bmatrix} \\ &= \begin{bmatrix} 1 & l \\ 0 & 1 \end{bmatrix} \begin{bmatrix} 1 & 0 \\ -1/f & 1 \end{bmatrix} \begin{bmatrix} 1 & f \\ 0 & 1 \end{bmatrix} \\ &= \begin{bmatrix} 1 & 0 \\ -1/f_{\text{RR}} & 1 \end{bmatrix} \begin{bmatrix} -1 & 0 \\ 0 & -1 \end{bmatrix}, \end{aligned} \quad (1)$$

where

$$f_{\text{RR}} = 1 / \left( \frac{2l}{f^2} - \frac{2}{f} \right). \quad (2)$$

From (1), the matrix  $\mathbf{M}_{\text{RR}}$  is equivalent to the combination of an imaging device (negative identity matrix) and a lens. If  $l = f$ , the matrix  $\mathbf{M}_{\text{RR}}$  exhibits the characteristic of an ideal telecentric cat's eye; that is

$$\mathbf{M}_{\text{RR}} \Big|_{l=f} = \begin{bmatrix} -1 & 0 \\ 0 & -1 \end{bmatrix}. \quad (3)$$

With the imaging characteristic of the ideal telecentric cat's eye depicted in (3), the output ray vector is expressed as

$$\begin{bmatrix} r_o \\ \alpha_o \end{bmatrix} = \mathbf{M}_{\text{RR}} \Big|_{l=f} \begin{bmatrix} r_i \\ \alpha_i \end{bmatrix} = \begin{bmatrix} -r_i \\ -\alpha_i \end{bmatrix}, \quad (4)$$

where  $r_o$  ( $r_i$ ) is the transverse displacement of the ray from the optical axis at the incidence plane; and  $\alpha_o$  ( $\alpha_i$ ) is the slope of the output (input) ray. According to (4), the output ray is always parallel to the input ray. This imaging characteristic supports the mobility of the spatially distributed resonator, i.e., two retroreflectors don't need to be aligned strictly to each other, since the intra-cavity rays from one retroreflector can always be reflected back by the other retroreflector.

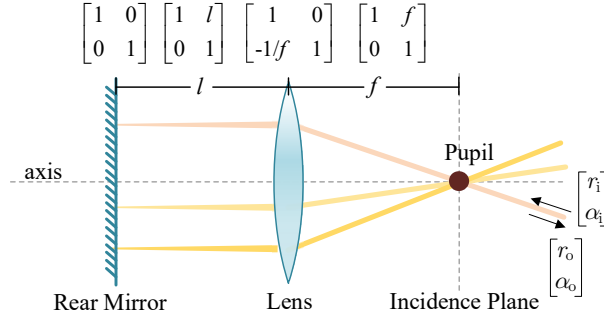


Fig. 4: Telecentric cat's eye retroreflector

### C. Spatially Separated Resonator

The spatially separated resonator consists of two telecentric cat's eye retroreflectors, as in Fig. 5. To build a stable resonator, the condition  $l > f$  (i.e.,  $f_{RR} > 0$ ) must be satisfied, so that  $\mathbf{M}_{RR}$  exhibits the capability of focusing light. ABCD matrices are used to analyze the stability of resonators and obtain the intensity distribution of transverse modes of the intra-cavity beam. The single-pass ABCD matrix of the resonator in Fig. 5 which describes the ray traveling from mirror M1 to mirror M2 is obtained as [19–21]

$$\begin{aligned}
 \begin{bmatrix} A & B \\ C & D \end{bmatrix} &= \begin{bmatrix} 1 & 0 \\ 0 & 1 \end{bmatrix} \begin{bmatrix} 1 & l \\ 0 & 1 \end{bmatrix} \begin{bmatrix} 1 & 0 \\ -\frac{1}{f} & 1 \end{bmatrix} \begin{bmatrix} 1 & 2f + d \\ 0 & 1 \end{bmatrix} \\
 &= \begin{bmatrix} 1 & 0 \\ -\frac{1}{f} & 1 \end{bmatrix} \begin{bmatrix} 1 & l \\ 0 & 1 \end{bmatrix} \begin{bmatrix} 1 & 0 \\ 0 & 1 \end{bmatrix} \\
 &= \begin{bmatrix} -1 - \frac{d}{f} + \frac{dl}{f^2} & 2f - 2l + d - \frac{2dl}{f} + \frac{dl^2}{f^2} \\ \frac{d}{f^2} & -1 - \frac{d}{f} + \frac{dl}{f^2} \end{bmatrix}. \tag{5}
 \end{aligned}$$

One can calculate the beam radius at the mirrors located at both ends of the resonator by the theory of equivalent resonator. From (5), the equivalent g-parameters  $\{g_1^*, g_2^*\}$  and the equivalent length  $L^*$  of the resonator is [21]

$$g_1^* = A = \frac{d}{2f_{RR}} - 1, \tag{6}$$

$$g_2^* = D = \frac{d}{2f_{RR}} - 1, \tag{7}$$

$$L^* = B = -\frac{f^2}{f_{RR}} + \frac{df^2}{4f_{RR}^2}. \tag{8}$$

From (8), the resonator can be described by three parameters  $\{d, f, f_{RR}\}$ . The value of  $l$  can be obtained if  $f$  and  $f_{RR}$  are known. The resonator is stable if the condition  $0 < g_1^* g_2^* < 1$  holds [21]. Therefore, we can derive the following stability condition for our resonator, namely

$$0 \leq d < 4f_{RR} \text{ and } d \neq 2f_{RR}. \tag{9}$$

Note that  $d = 2f_{\text{RR}}$  is also acceptable, where the equivalent resonator is a confocal cavity which exhibits the best stability.

According to laser principle, the fundamental mode,  $\text{TEM}_{00}$ , in a stable resonator is a Gaussian beam. The  $\text{TEM}_{00}$  mode radius at mirror M1 is obtained as [21, 22]

$$w_{00}(0) = \sqrt{\frac{\lambda |L^*|}{\pi} \sqrt{\frac{g_2^*}{g_1^*(1 - g_1^*g_2^*)}}}, \quad (10)$$

where  $\lambda$  is the wavelength of the beam, and  $\pi$  is the ratio of a circle's circumference to its diameter.

The parameters of the Gaussian beam propagating inside the resonator can be obtained according to the fact that mirror surfaces are the constant-phase surfaces for the beam [21]. Since the ROC of M1 is infinite, the ROC of the constant-phase surface of the beam at M1 is also infinite, which means the waist of the beam between M1 and L1 locates at M1, as only the constant-phase surface at the waist of the Gaussian beam exhibits infinite ROC. Once we obtain the waist radius of the Gaussian beam, we can obtain its  $g$ -parameter as a function of the location along the  $z$ -axis. Then, we can compute the mode radius at any location inside or outside the resonator. Finally, the  $q$ -parameter at M1 is [21]

$$q_0 = j \frac{\pi w_{00}^2(0)}{\lambda}, \quad (11)$$

where  $j := \sqrt{-1}$ . By using the ray-transfer matrix, i.e. the ABCD law [21], the  $q$ -parameter along the axis is obtained as

$$q(z) = \begin{cases} q_0 + z, & z \in [0, z_{L1}] \\ \frac{q(z_{L1})}{-q(z_{L1})/f + 1} + (z - z_{L1}), & z \in (z_{L1}, z_{L2}] \\ \frac{q(z_{L2})}{-q(z_{L2})/f + 1} + (z - z_{L2}), & z \in (z_{L2}, z_{M2}] \end{cases} \quad (12)$$

where  $z_{L1} = l$ ,  $z_{L2} = l + 2f + d$ , and  $z_{M2} = 2l + 2f + d$ . The Gaussian beam radius  $w_{00}(z)$  at the location  $z$  is determined by the imaginary parts of  $1/q(z)$ , namely [21]

$$w_{00}(z) = \sqrt{-\frac{\lambda}{\pi \Im[1/q(z)]}}, \quad (13)$$

where  $\Im[\cdot]$  takes the imaginary part of a complex quantity.

Next, we consider the higher-order transverse modes,  $\text{TEM}_{mn}$ , in the resonator. These higher-order modes have a larger radius than  $\text{TEM}_{00}$  mode. All these modes are superposed together, forming an intra-cavity resonant beam. The beam radius  $w(z)$  at an arbitrary location is calculated by [21]

$$w(z) = w_{00}(z)M, \quad (14)$$

where  $M$  is the beam propagation factor. Since the gain medium aperture is much smaller than that of other mirrors and lens in the cavity, the beam propagation factor can, to a good approximation, be calculated with [21]

$$M = \frac{a_g}{w_{00}(l + f)}, \quad (15)$$

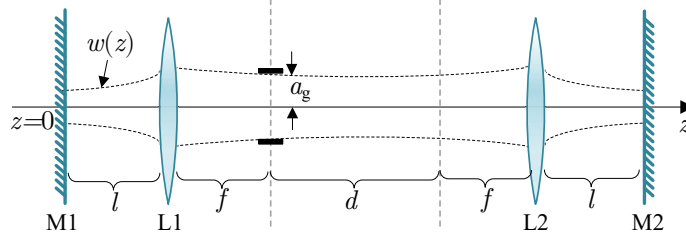


Fig. 5: Schematic of intra-cavity beam radius distribution

where  $a_g$  is the radius of the gain medium aperture, and  $w_{00}(l+f)$  is the radius of  $TEM_{00}$  mode at the location of the gain medium. The mode index  $m$  and  $n$  are limited by [21]

$$2m + n + 1 \leq M^2. \quad (16)$$

#### D. Fundamental Beam Generation

As depicted in Fig. 6, photons oscillate in the resonator and are amplified by the gain medium, forming the resonant beam. A portion of the resonant beam is extracted by M4 as the fundamental beam for SHG. In this part, we create the mathematical model to calculate the power of the extracted fundamental beam.

The resonance can be built when the threshold condition is met; that is [23]

$$2g_0l_g \geq \delta, \quad (17)$$

where  $g_0$  is the small-signal gain coefficient of the gain medium,  $l_g$  is the path length of the beam internal the gain medium, and  $\delta$  is the total round-trip loss coefficient of the resonator. The small-signal gain coefficient is determined by the power density of the pump light absorbed by the gain medium, namely [23]

$$g_0 = \frac{\eta_c P_{in}}{I_s V}, \quad (18)$$

where  $I_s = (h\nu)/(\sigma_s \tau_f)$  is the saturation intensity;  $\nu = c/\lambda$  is the wavelength of the intra-cavity beam;  $\sigma_s$  and  $\tau_f$  are the stimulated emission cross section and the fluorescence time of the gain medium, respectively;  $P_{in}$  is the electrical power used for driving the pump laser diodes; and  $V$  is the volume of the gain medium. The combined pumping efficiency  $\eta_c$  is expressed as [23]

$$\eta_c = \eta_P \eta_t \eta_a \eta_Q \eta_S \eta_B, \quad (19)$$

where  $\eta_P$  is the pump source generation efficiency,  $\eta_t$  is the pump source transfer efficiency,  $\eta_a$  is the pump source absorb efficiency,  $\eta_Q$  is the quantum efficiency,  $\eta_S = \nu/\nu_p$  is the Stokes factor,  $\nu_p$  is the pump light frequency, and  $\eta_B$  is the overlap efficiency defined as the ratio of the mode volume of the resonant beam to the volume of the active gain medium.

The losses in the resonator include reflection loss, transmission loss, absorption loss, scattering loss, and diffraction loss. These losses are induced by mirrors, lenses, the gain medium, and the air-transmission. The total round-trip loss coefficient is defined as

$$\delta = -\ln(\Gamma_{\text{RR1}}\Gamma_{\text{diff}}\Gamma_{\text{g}}\Gamma_{\text{M4}}\Gamma_{\text{air}}\Gamma_{\text{RR2}}), \quad (20)$$

where  $\Gamma_{\text{RR1}}$ ,  $\Gamma_{\text{RR2}}$ ,  $\Gamma_{\text{g}}$ , and  $\Gamma_{\text{air}}$  are the round-trip loss factors induced by RR1, RR2, the gain medium, and the air, respectively;  $\Gamma_{\text{M4}} = 1 - R_4$  is the transmissivity of M4 at 1064 nm;  $\Gamma_{\text{diff}}$  is the round-trip diffraction loss factor. The round-trip air-transmission loss factor is expressed as [24]

$$\Gamma_{\text{air}}(d) = e^{-2\alpha_{\text{air}}d}, \quad (21)$$

where  $\alpha_{\text{air}} = 10^{-4} \text{ m}^{-1}$  is the loss coefficient of clear air, and  $d$  is the transmission distance.

Next, we compute the power of the fundamental beam extracted by M4. According to Rigrod analysis, for the simplest resonator with only two mirrors and one gain medium lied between the two mirrors, the intensity of the rightward-traveling light at the right mirror is computed by [25]

$$I_+ = \frac{I_s}{(1 + r_2/r_1)(1 - r_1r_2)} \left[ g_0 l_{\text{g}} - \ln \frac{1}{r_1 r_2} \right], \quad (22)$$

where  $r_1 \equiv \sqrt{\mathcal{R}_1}$  and  $r_2 \equiv \sqrt{\mathcal{R}_2}$  are the voltage reflection coefficients of the mirrors; and  $\mathcal{R}_1$  and  $\mathcal{R}_2$  are the reflectivity of the mirrors.

In our system model, we combine all the loss factors into two equivalent reflectance  $\mathcal{R}_1$  and  $\mathcal{R}_2$ , as demonstrated in Fig. 6. Considering the receiver's orientation angle  $\{\alpha, \beta\}$  and attitude angle  $\{\theta, \phi\}$  [26], we use  $\mathcal{R}_1(\zeta, d)$  to denote the equivalent reflectivity for the combined loss induced by RR1, the diffraction loss, and the gain medium; that is

$$\mathcal{R}_1(\zeta, d) = \Gamma_{\text{RR1}}(\zeta)\Gamma_{\text{g}}(\zeta)\Gamma_{\text{diff}}(\zeta, d), \quad (23)$$

where  $\zeta = [\alpha, \beta, \theta, \phi]$ , and  $d$  is the transmission distance.  $\mathcal{R}_2(\zeta)$  denotes the equivalent reflectivity for the combined loss induced by M4, the air, and RR2; that is

$$\mathcal{R}_2(\zeta, d) = \Gamma_{\text{M4}}(\zeta)\Gamma_{\text{air}}(d)\Gamma_{\text{RR2}}(\zeta). \quad (24)$$

The intensity of the leftward-traveling light on the left surface of M4 is expressed as

$$I_- = \mathcal{R}_2(\zeta, d)I_+. \quad (25)$$

Then the intensity of the fundamental beam extracted by M4 is obtained as

$$I_{\nu}(\zeta, d) = \frac{R_4(\zeta)}{1 - R_4(\zeta)} I_- = \frac{\mathcal{R}_2(\zeta, d)R_4(\zeta)}{1 - R_4(\zeta)} I_+, \quad (26)$$

where  $R_4(\zeta)$  is the reflectivity of M4 at the frequency  $\nu$ . From (18), (22), and (26), the average power of the extracted fundamental beam is then obtained as

$$\begin{aligned} P_{\nu}(\zeta, d) &= A_{\text{g}}(\zeta)I_{\nu}(\zeta, d) \\ &= \eta_{\nu}(\zeta, d)[P_{\text{in}} - P_{\text{th}}(\zeta, d)] \end{aligned} \quad (27)$$

where

$$\eta_\nu(\zeta, d) = \frac{l_g(\zeta)\eta_c(\zeta, d)A_g(\zeta)\mathcal{R}_2(\zeta, d)R_4(\zeta)}{V[1 - R_4(\zeta)]\left[1 + \frac{r_2(\zeta, d)}{r_1(\zeta, d)}\right][1 - r_1(\zeta, d)r_2(\zeta, d)]}, \quad (28)$$

and

$$P_{\text{th}}(\zeta, d) = \ln\left[\frac{1}{r_1(\zeta, d)r_2(\zeta, d)}\right] \cdot \frac{I_s V}{l_g(\zeta)\eta_c(\zeta)}. \quad (29)$$

Here  $A_g(\zeta)$  represents the beam cross section area at the gain medium, and  $l_g(\zeta)$  is the path length of the beam internal the gain medium. Note that, among all the efficiency components of  $\eta_c(\zeta, d)$ , only the overlap efficiency  $\eta_B(\zeta, d)$  is relevant to  $\zeta$  and  $d$ . We only consider multi-mode oscillation, as the apertures of the devices in the cavity are much greater than the cross section of the  $\text{TM}_{00}$  mode; and on this condition, the beam can be assumed to have uniform transversal intensity pattern. Therefore, we neglect the parameter  $\zeta$  and  $d$ , and use  $\eta_c$  and  $\eta_B$  to denote the combined pumping efficiency and the overlap efficiency, respectively.

Well-designed AR/HR coating has extremely high transmittance/reflectivity within a large angle of incidence (generally,  $> 99\%$ , within  $\pm 10^\circ$ ). The diffraction loss depends on the location of the receiver. The diffraction loss can be calculated by numerical simulation program (for example, the Fox-Li algorithm) [27]. In the following, we only consider the special case, where  $\zeta = [0, 0, 0, 0]$ , because the optimum performance is achieved at the direction along the optical axis. According to (27), the closed-form propagation model can be expressed as

$$P_\nu(d) = \eta_\nu(d)[P_{\text{in}} - P_{\text{th}}(d)] \quad (30)$$

For calculating the explicit fundamental beam power expressed by (30), the diffraction loss can be computed by the model presented in Appendix A. For simplicity, we also assume optimum shape of gain medium. In this case, the radius of beam cross section at the gain medium  $A_g = \pi a_g^2$ , where  $a_g$  is the radius of the gain medium aperture. Besides, the beam path length internal the gain medium  $l_g$  is approximate to the gain medium thickness.

### E. Second Harmonic Generation

The fundamental beam passes through lens L3 and then enters the SHG medium. After that, the frequency-doubled beam is generated. SHG is a nonlinear optical process, in which two photons with the same frequency interact with the SHG medium to generate a new photon with twice the frequency and energy of the original photon. Some birefringent crystals are capable of generating frequency-doubled beam, such as potassium titanyl phosphate (KTP), potassium dihydrogen phosphate (KDP), and lithium niobate ( $\text{LiNbO}_3$ ).

The SHG efficiency is determined by the input fundamental beam intensity (power  $P_\nu$  divided by beam cross section  $A_\nu$ ) and the length of the SHG medium  $l_s$ . Here we assume the fundamental beam is a plane-wave beam with critical phase matching and the effect of walk-off is neglected. Thus, the power of the frequency-doubled beam is obtained as [23, 28]

$$P_{2\nu} = \frac{K l_s^2 P_\nu^2}{A_\nu}, \quad (31)$$

where

$$K = \frac{8\pi^2 d_{\text{eff}}^2}{\varepsilon_0 c \lambda^2 n_0^3}, \quad (32)$$

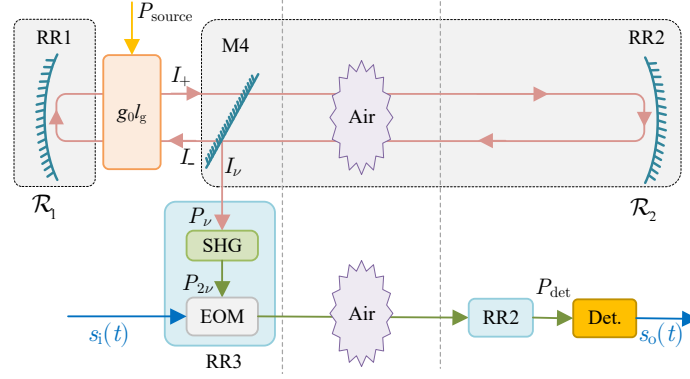


Fig. 6: Power and signal flow

$d_{\text{eff}}$  is the efficient nonlinear coefficient of the SHG medium,  $\varepsilon_0$  is the vacuum permeability,  $c$  is the light speed,  $n_0$  is the refractive index of the SHG medium, and  $A_\nu$  is the cross section area of the fundamental beam that enters the SHG medium. Supposing the output surface of SHG medium is attached to M3, and neglecting the thickness of the EOM, we obtain  $A_\nu = \pi w^2(l_s)$  according to (14). Note that the plane-wave approximation is valid only when the length of SHG medium  $l_s$  is smaller than the Rayleigh length ( $z_R = \pi w_0^2(0)/\lambda$ ) of the fundamental beam.

For each incident frequency, a specific phase matching angle should be satisfied for SHG progress. Otherwise, the conversion efficiency would be extremely low. Therefore, in our system, the SHG effect is neglected for the modulated beam reflected back by M3, as the phase matching angle is set specifically for the fundamental frequency.

#### F. Communication Channel Model

The frequency-doubled beam is modulated by the EOM to carry information. Then the modulated beam travels along the path of the original fundamental beam to be received by the PD. The received optical power at the PD is

$$\hat{P}_r = \eta_{\text{dev}} \Gamma_{\text{air}}^{1/2} P_{2\nu}, \quad (33)$$

where  $\eta_{\text{dev}}$  is the combined transmission efficiency of all the devices that the modulated beam passes through, including EOM, the SHG medium, L1, M4, RR2, L4, and the PD. Note that  $\hat{P}_r$  represents the peak power of the optical signal.

Wireless optical communications can be modeled as a linear time-invariant system [3]. Let  $s_i(t)$  denote the source signal to be transmitted. The detected current signal at the receiver is expressed as

$$s_o(t) = \gamma P_{2\nu} s_i(t) * h(t) + n(t), \quad (34)$$

where  $*$  is the convolution operator,  $\gamma$  is the PD's responsivity, and  $n(t)$  denotes the additive white Gaussian noise (AWGN).  $h(t)$  is the channel impulse response of the transmission from the modulator to the detector, which is expressed as

$$h(t) = h_{\text{EOM}}(t) * h_{\text{air}}(t) * h_{\text{det}}(t), \quad (35)$$

TABLE I: Resonator Parameters [23, 29]

Parameter	Symbol	Value
Stimulated emission cross section	$\sigma$	$15.6 \times 10^{-23} \text{ m}^2$
Fluorescence lifetime	$\tau_f$	100 $\mu\text{s}$
Fundamental beam wavelength	$\lambda$	1064 nm
Radius of gain medium aperture	$a_g$	3 mm
Gain medium thickness	$l_g$	1 mm
Quantum efficiency	$\eta_Q$	95%
Stocks factor	$\eta_S$	76%
Overlap efficiency	$\eta_B$	90%
Pump source efficiency	$\eta_P$	75%
Pump source transfer efficiency	$\eta_t$	99%
Absorb efficiency	$\eta_a$	91%

TABLE II: Second Harmonic Generation Parameters [23]

Parameter	Symbol	Value
Efficient nonlinear coefficient	$d_{\text{eff}}$	4.7 pm/V
refractive index	$n_0$	2.23
SHG medium length	$l_s$	2 mm

where  $h_{\text{EOM}}(t)$ ,  $h_{\text{air}}(t)$ , and  $h_{\text{det}}(t)$  are the impulse response functions of the EOM, the air-transmission channel and the PD, respectively. The effects on frequency domain imposed by the optics and air transmission channel can be neglected, as the bandwidth of the baseband signal is very narrow compared with the light frequency.

The noises include the pump source noise, the background light noise, the PD noise, and the demodulating noise. However, since the gain medium acts like a capacitor, only low-frequency noise from the pump source can be transferred to the receiver, which is out of the communication band and can be easily filtered. The background light noise can be filtered by an optical filter. Besides, well-designed demodulation circuits can dramatically reduce the noise and amplify the signal. Only the Gaussian white noise generated by photo-detector is considered, because the receiving power is great so that the shot noise and the thermal noise of the photodetector are dominant among these noise factors.

According to the classic literature, the channel capacity of our system is computed by [30]

$$\tilde{C} = \log_2(1 + SNR), \quad (36)$$

where the signal-to-noise ratio  $SNR$  is obtained as

$$SNR = \frac{(\gamma P_r)^2}{\sigma_{\text{total}}^2}, \quad (37)$$

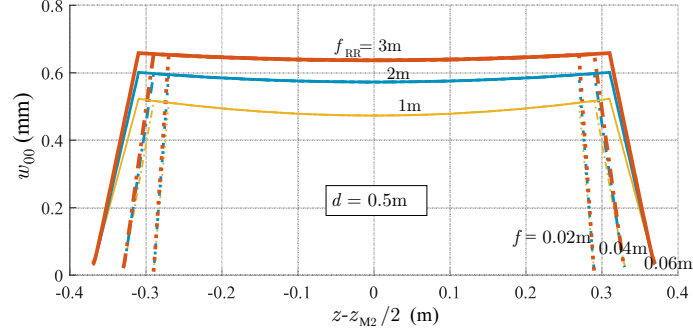


Fig. 7: Beam radius of TEM<sub>00</sub> mode along the resonator's axis for different  $f_{RR}$  and focal length  $f$  ( $z_{M2} = 2l + 2f + d$  is the resonator's length for each case)

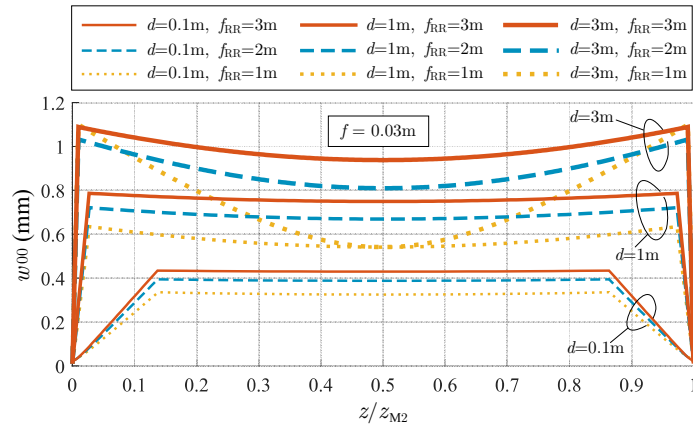


Fig. 8: Beam radius of TEM<sub>00</sub> mode along the resonator's axis for different  $f_{RR}$  and distance  $d$  ( $z/z_{M2}$  is the normalized  $z$ -coordinate, where  $z_{M2} = 2l + 2f + d$  is the resonator's length for each case)

where  $P_r < \hat{P}_r$  is the average received optical signal power. The significant noises power includes the thermal noise power and the shot noise power of the PD; that is [31]

$$\sigma_{\text{total}}^2 = \sigma_{\text{shot}}^2 + \sigma_{\text{thermal}}^2. \quad (38)$$

The shot noise power ( $A^2$ ) is given by

$$\sigma_{\text{shot}}^2 = 2e(\gamma P_r + I_{\text{bk}})B, \quad (39)$$

where  $e$  is the electron charge,  $I_{\text{bk}} = 5100 \mu\text{A}$  is the background radiation induced photocurrent [32], and  $B$  is the bandwidth of PD. The thermal noise power ( $A^2$ ) is given by

$$\sigma_{\text{thermal}}^2 = \frac{4kTB}{R_L}, \quad (40)$$

where  $k$  is the Boltzmann constant,  $T$  is the absolute temperature, and  $R_L$  is the load resistor.

TABLE III: Technology Comparison

Work	Transmitter	Distance	Achievable Rate	Beam Diameter	Mobile Scheme	Positioning
Wang <i>et al.</i> [5]	wavelength swept laser	1.4 m	12 Gbit/s	-	tilted fiber grating	need
Sung <i>et al.</i> [4]	XFP transceiver	1.7 m	10 Gbit/s	114 mm	fiber array	need
Rhee <i>et al.</i> [7]	monochromatic laser diode	3m	32 Gbit/s	42 mm	optical phase array	need
Chun <i>et al.</i> [8]	four-color laser diode	4 m	35 Gbit/s	10 mm	MEMS mirror	need
This work	RBCom system	8 m	11.2 Gbit/s	6 mm	self-alignment	don't need

### III. PERFORMANCE EVALUATION

In this section, we analyze the beam radius, the power of the fundamental beam, and the channel capacity of the proposed RBCom system. We set  $P_r = \hat{P}_r$  to obtain the upper bound of the achievable channel capacity. The gain medium is an Nd:YVO<sub>4</sub> crystal. The parameters of the resonator are listed in Table I. Considering  $\zeta = [0, 0, 0, 0]$ , the loss factors  $\Gamma_{RR1}$ ,  $\Gamma_{RR2}$ ,  $\Gamma_g$ , and  $\eta_{dev}$  are set to 1. An LiNbO<sub>3</sub> crystal is employed as the SHG medium, as it has high nonlinear coefficient and 0° walk-off angle at 1064 nm; its parameters are specified in Table II. Besides, we consider the channel bandwidth is determined by the bandwidth of the modulator, thus, we set  $B = 800$  MHz [33]. The PD's responsivity  $\gamma = 0.6$  A/W. The temperature  $T = 295$  K. The load resistor connected to the PD is  $R_L = 10$  k $\Omega$  [31, 34].

#### A. Beam Radius

Figure 7 shows the beam radius  $w_{00}$  of the TEM<sub>00</sub> mode distributed along the resonator's axis for the transmission distance  $d = 0.5$  m. The beam radius are symmetric about the half-distance position  $z = z_{M2}/2$ . Besides,  $w_{00}$  reaches the minimum on mirrors M1 and M2, and reaches the maximum on lenses L1 and L2. The beam waist (the position where the Gaussian beam reaches the smallest radius) in the free space is located at the half-distance position. Moreover, as  $f_{RR}$  increases, the beam radius in the free space increases. Besides, the focal length  $f$  has less effect on the beam radius profile in the free space if  $f_{RR}$  is specified.

We also analyzed the relationship between the beam radius profile and the resonator parameters including  $d$  and  $f_{RR}$ , for a certain  $f = 0.03$  m. In Fig. 8, with the same  $d$ , a greater  $f_{RR}$  results in a larger beam waist  $w_{00}$  in the free space. With a given  $f_{RR}$ , as distance  $d$  increases, the beam radius  $w_{00}$  near the lens and the gain medium becomes larger. This analysis reveals the fact that the intra-cavity beam is always focused onto the receiver under the stable state, so the received power as well as the channel capacity can reach a considerable level. As depicted in (16), a larger TEM<sub>00</sub> mode radius  $w_{00}$  leads to a smaller mode number, which indicates a higher diffraction loss, a more inhomogeneous transverse intensity distribution, and a smaller overlap efficiency. Therefore, a gain medium with large cross section is required if we design a long-distance communication system.

#### B. Power of Fundamental Beam

Figure 9 shows the power  $P_\nu$  of the fundamental beam as a function of the reflectivity  $R_4$  of the coating M4, for different electrical driving power  $P_{in}$  and a certain transmission distance  $d = 5$  m. As  $R_4$  increases,  $P_\nu$

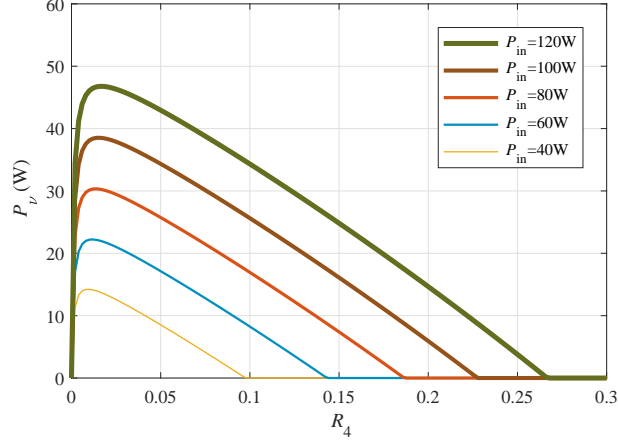


Fig. 9: Fundamental beam power  $P_\nu$  vs. splitter's reflectivity  $R_4$  (transmission distance  $d = 5$  m, focal length of lens  $f = 0.03$  m,  $f_{RR} = 3$  m)

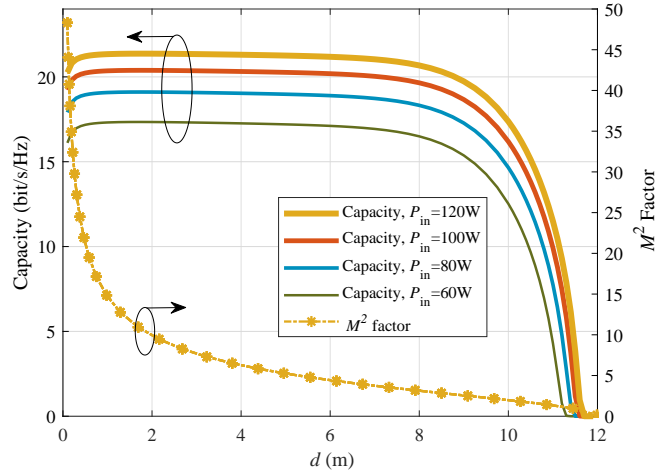


Fig. 10: Channel capacity  $\tilde{C}$  and  $M^2$  factor vs. transmission distance  $d$  (reflectivity  $R_4 = 0.02$ , focal length of lens  $f = 0.03$  m,  $f_{RR} = 3$  m)

increases rapidly at first and then decreases to 0 gradually. The maximum  $P_\nu$  can be obtained with a specific  $R_4$ . For instance, when  $P_{in} = 100$  W, the maximum  $P_\nu$  can be obtained when  $R_4$  is close to 2%. Moreover, as  $P_{in}$  grows, the optimal value of  $R_4$  appears slightly increasing.

### C. Communication Performance

We evaluated the communication capacity at different distance  $d$ . As depicted in Fig. 10, the channel capacity exhibits less difference for  $d < 8$  m. As  $d$  grows from 8 m to 12 m, the capacity decreases to 0 quickly. Furthermore, it is obvious that the  $M^2$  factor keeps greater than 4 for  $d < 6$  m, which indicates that at least 6 transverse modes are oscillating together. In this case, the intra-cavity fundamental beam has a homogeneous transverse intensity

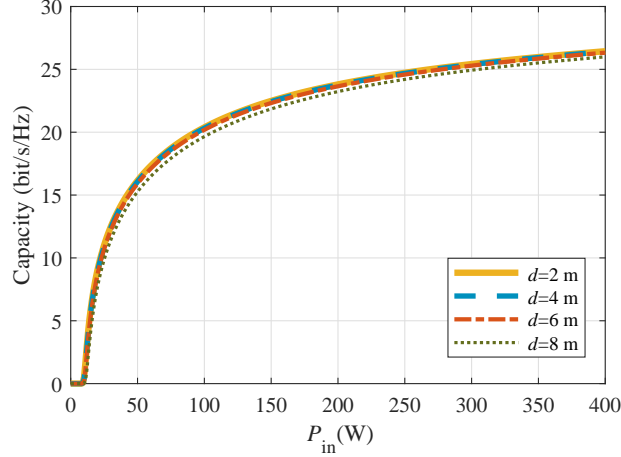


Fig. 11: Channel capacity  $\tilde{C}$  vs. electrical driving power  $P_{\text{in}}$  ( $R_4 = 0.02$ , focal length of lens  $f = 0.03$  m,  $f_{\text{RR}} = 3$  m)

distribution. When  $d$  approaches 12 m, the resonator turns to unstable state and the  $\text{TEM}_{00}$  mode radius  $w_{00}$  is greater than the gain medium radius (no matter how large the gain medium is). Therefore, the diffraction loss becomes so significant that no mode can keep oscillating. When the distance increases within 8 m, the channel capacity decreases slightly.

Figure 11 depicts the relationship between the channel capacity and the electrical driving power  $P_{\text{in}}$ . There is a threshold of  $P_{\text{in}}$  for each case. If  $P_{\text{in}}$  is below the threshold, the resonance has not been established, and thus the capacity is 0. After  $P_{\text{in}}$  exceeding the threshold, the channel capacity increases rapidly. Moreover, the growth rate of the capacity reduces gradually as  $P_{\text{in}}$  increases. When the electrical driving power is 100 W and the distance is 8 m, the channel capacity is 19.7 bit/s/Hz. However, the channel capacity only increases to 26 bit/s/Hz as the driving power reaches 400 W. Within this range of driving power, the maximum detected power at the receiver is 35.4 mW. Compared with the fundamental beam power depicted in Fig. 9, the SHG efficiency is low. Even though, the achievable power level is enough for communication, while common LED-based VLC or laser communication systems generally receive less than 1 mW due to beam divergence and/or safety issues [35].

In addition, quadrature amplitude modulation (QAM) and orthogonal frequency division multiplexing (OFDM) schemes are adopted in simulation to evaluate the communication performance. The QAM order is 16384, which means each QAM symbol transmits 14 bit. The OFDM signal contains 800 subcarriers and is transmitted through 800-MHz channel. The fast Fourier transform (FFT) length is 1024. The cyclic prefix length is 176. Besides, digital clipping is adopted to reduce the peak to average power ratio. Since the optical channel is a nonnegative real channel, the transmitted OFDM signal is biased by a direct-current (DC) signal. Result shows that when the pump source power is 120 W and the transmission distance is 8 m, the data rate reaches 11.2 Gbit/s with bit error rate (BER)  $< 3.8 \times 10^{-3}$ . The beam diameter at the receiver is approximate to 6 mm. Table III demonstrates the distinction between our system and the state-of-art architectures.

## IV. DISCUSSION

### A. Channel Bandwidth

According to (35), the channel bandwidth is determined by the minimum bandwidth among which of the EOM, the air-transmission channel and the PD. For indoor application with intensity-modulation/direct-demodulation (IM/DD) scheme, the frequency characteristic of the air-transmission channel can be modeled as a direct-current (DC) gain. The multiple quantum well (MQW) EOM with bandwidth up to 37 GHz was reported in [36], which is higher than most of other EOMs. Generally, the modulating speed is limited by EOM's capacitance. Reducing the active area or increasing the intrinsic region thickness can decrease the capacitance. Thus, to produce a high-speed MQW EOM, we split the active area into small pixels. To reduce the power consumption, we can only select irradiated pixels for modulation operation, which benefits from the fact that the MQW can also perform as a PD if reversely biased [37]. Similar to the MQW EOM, the response speed of the PD is also determined by its diode's capacitance. For high speed communications with a large receiving aperture, PD arrays with small area are the best choice [38], or one can adopt a lens to focus the light onto an independent small detector [39]. Commercially available PDs generally have bandwidth up to 20 GHz [38].

### B. Power Efficiency

In order to improve the power efficiency, we can employ gain mediums with high saturated intensity and reduce the loss from the pumping progress. In this paper, we adopt an Nd:YVO<sub>4</sub> gain medium, as it has a high saturated intensity and is widely used in practice [40]. A better scheme is to employ semiconductor gain mediums which can be pumped directly with electricity so as to achieve a high efficiency [41]. Besides, the gain medium's efficiency can be improved by reducing the gain medium radius; this way also improves the SHG efficiency, since a smaller gain medium cross section provides a smaller beam spot and a higher beam intensity. Although reducing the gain medium radius will increase the diffraction loss and decrease the overlap efficiency simultaneously, this issue can be addressed by adding optics to minify the TEM<sub>00</sub> mode radius in the gain medium. For example, one can design a coupled cavity with an internal focal lens [42]. To improve the SHG efficiency, the SHG medium length is supposed to be extended. Yet, this method also leads to a greater retroreflector length, so it can be implemented for some applications without the needs of small assembly size.

### C. Carrier Wavelength

Most long-range FSO systems operate in the wavelength windows of 780–850 nm and 1520–1600 nm, in order to ensure attenuation < 0.2 dB/km [43]. These windows are nicely suitable to our system, as the former lies in the second-harmonic band of the latter. Although 532-nm carrier was demonstrated in our system, most of the preferable wavelengths can be obtained by replacing the gain material, especially, with semiconductor devices [38, 40].

### D. Resonance Stability

The fluctuation origins from two aspects: 1) Some device parameters change while moving; for example, the reflectivity of mirrors varies with the incident angle, which induces slow power fluctuation of the intra-cavity beam;

and 2) the balance condition of the resonance system is broken so that the oscillation turns into unstable state. In terms of the first aspect, the moving speed of the devices is quite slow, compared with the signal's swinging speed. This effect can be overcome easily by many common schemes adopted by the existing communication system, for example, automatic gain control (AGC) [44]. In terms of the second aspect, due to the open-cavity structure, moving and atmospheric turbulence can break the balance condition of the resonance, which leads to intensity fluctuation of the fundamental beam. This phenomenon is called relaxation oscillation in literature. The oscillation frequency and the dumping time depend on the pumping rate, the upper-level atoms lifetime, and the cavity photons lifetime [25]. Slow-frequency and small-amplitude oscillation can be achieved by supplying an adequate electrical driving power that is just above the threshold. Some signal processing and coding schemes can also be introduced to overcome the impacts brought from relaxation oscillation. Besides, a more effective way to suppress fluctuation is adopting optoelectronic feedback controlling [45], especially for solid-state laser which usually fluctuates at a few kHz [46]. This scheme does not need channel information estimation, but only needs to detect the intra-cavity beam power at the transmitter and correspondingly control the pump source power.

#### *E. Uplink Communication*

Uplink communication can be realized by improving the system design. For example, an extra SHG medium is mounted at the receiver with correct phase matching angle. Thus, the fourth harmonic beam can be acquired, which acts as the uplink communication carrier. Or we can design a receiver identical to the transmitter, excluding the gain medium, to generate a second harmonic beam. Moreover, we can mount liquid shutters between the real mirror and the EOM at both the transmitter and receiver to switch the beam propagating path. Uplink communication can be realized by closing the transmitter's shutter and opening the receiver's shutter, which only allows the second harmonic beam to propagate from the receiver to the transmitter.

### V. CONCLUSIONS

In this paper, we aimed at dealing with the echo-interference issue in the RBCom system. We at first proposed an echo-interference-free RBCom system design which exploits SHG to produce frequency-doubled carrier beam for communications. Next, we established an analytical model of the proposed system. Moreover, we evaluated the beam radius in the resonator and the channel capacity of the RBCom system. Communication simulation with OFDM scheme was conducted. The results show that our system achieves longer transmission distance and smaller beam diameter for transmission beyond 10 Gbit/s, compared with the existing OWC technologies. Besides, the existing technologies need positioning program, while our system avoids the positioning progress with the aid of its self-alignment feature. Further studies on the mobility and stability and the approach of improving the power efficiency are well motivated.

### APPENDIX A

#### DIFFRACTION LOSS APPROXIMATION

Obtaining diffraction loss of the spatially separated laser resonator which consists of several elements and an internal aperture is complicated generally through numerical method. Here we provide a method to obtain an

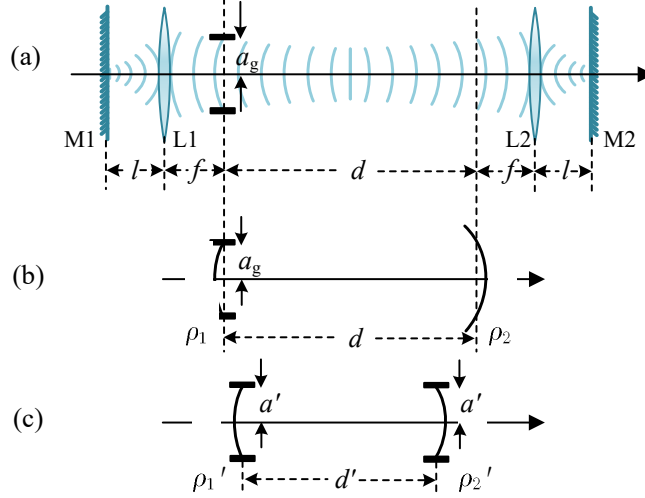


Fig. 12: Equivalent resonator for diffraction loss calculation

approximate solution. Note that all the diffraction loss are assumed to be caused by the gain medium, as its aperture is much smaller than that of other lenses and mirrors in the system.

As depicted in Fig. 12(a), the total diffraction loss for a round-trip is composed of the diffraction losses on the two sides of the aperture. From (1), the retroreflector placed on the left side of the gain medium has a vanished B-element in its ray transfer matrix. For this kind of system, its diffraction loss can be neglected [47].

Then we create an equivalent empty resonator to obtain the diffraction loss on the right surface of the gain medium, as shown in Fig. 12(b). The mirrors surface of the equivalent resonator is assumed identical to the constant-phase surface of the original intra-cavity beam at two selected locations, i.e., the location of the gain medium (located at the pupil of the retroreflector RR1) and the pupil of the retroreflector RR2. Thus, the length of the equivalent resonator is  $d$ .

According to the formula for calculating the ROC of the constant-phase surface of a Gaussian beam, the ROCs of the mirrors of the equivalent resonator is obtained as [21]

$$\rho_1 = -\frac{1}{\Re[1/q(l+f)]}, \quad \rho_2 = \frac{1}{\Re[1/q(l+f+d)]}, \quad (41)$$

where  $\Re[\cdot]$  takes the imaginary part of a complex quantity. The resonator with one finite-aperture mirror and one infinite-aperture mirror is equivalent to another symmetric resonator with two identical apertures at both mirrors, as depicted in Fig. 12(c). The equivalent Fresnel number  $N'$  and g-parameters  $\{g'_1, g'_2\}$  are [19]

$$N' = \frac{a_g^2}{2\lambda d \left(1 - \frac{d}{\rho_2}\right)},$$

$$g'_1 = g'_2 = 1 - 2d \left( \frac{1}{\rho_1} + \frac{1}{\rho_2} - \frac{d}{\rho_1 \rho_2} \right). \quad (42)$$

Note that the Fresnel number taking a negative value is acceptable, as it only indicates the change of the phase rather than the intensity pattern [48]. Then, the round-trip diffraction loss factor of the TEM<sub>00</sub> mode is approximated

by [49]

$$\Gamma_{\text{diff}} = 1 - \exp \left[ -2\pi |N'| \sqrt{\frac{g'_1(1 - g'_1 g'_2)}{g'_2}} \right]. \quad (43)$$

In this paper, we only analyze the diffraction loss of the  $\text{TEM}_{00}$  mode, as it determines the threshold of the resonance. In fact, for the operations with multiple transverse modes, the diffraction loss is small and negligible.

#### REFERENCES

- [1] K. David and H. Berndt, “6G vision and requirements: Is there any need for beyond 5G?” *IEEE Veh. Technol. Mag.*, vol. 13, no. 3, pp. 72–80, July 2018.
- [2] A. Jovicic, J. Li, and T. Richardson, “Visible light communication: opportunities, challenges and the path to market,” *IEEE Commun. Mag.*, vol. 51, no. 12, pp. 26–32, Dec. 2013.
- [3] A. Al-Kinani, C. Wang, L. Zhou, and W. Zhang, “Optical wireless communication channel measurements and models,” *IEEE Commun. Surveys Tuts.*, vol. 20, no. 3, pp. 1939–1962, May 2018.
- [4] J. Sung, F. G. Agis, A. Trinidad, E. Tangdiongga, and T. Koenen, “Coordinated multi-source (CoMS) transmission for optical wireless communications (OWC),” in *2018 European Conference on Optical Communication (ECOC)*, Rome, Italy, Nov. 2018, pp. 1–3.
- [5] G. Wang, U. Habib, Z. Yan, N. J. Gomes, Q. Sui, J.-B. Wang, L. Zhang, and C. Wang, “Highly efficient optical beam steering using an in-fiber diffraction grating for full duplex indoor optical wireless communication,” *J. Lightw. Technol.*, vol. 36, no. 19, pp. 4618–4625, Oct. 2018.
- [6] Z. Zhang, J. Dang, L. Wu, H. Wang, J. Xia, W. Lei, J. Wang, and X. You, “Optical mobile communications: Principles, implementation, and performance analysis,” *IEEE Trans. Vehi. Technol.*, Nov. 2019.
- [7] H. Rhee, J. You, H. Yoon, K. Han, M. Kim, B. G. Lee, S. Kim, and H. Park, “32 Gbps data transmission with 2D beam-steering using a silicon optical phased array,” *IEEE Photon. Technol. Lett.*, vol. 32, no. 13, pp. 803–806, May 2020.
- [8] H. Chun, A. Gomez, C. Quintana, W. Zhang, G. Faulkner, and D. OBrien, “A wide-area coverage 35Gb/s visible light communications link for indoor wireless applications,” *Sci. Rep.*, vol. 9, no. 1, Mar. 2019.
- [9] Q. Wu and R. Zhang, “Intelligent reflecting surface enhanced wireless network via joint active and passive beamforming,” *IEEE Trans. Wireless Commun.*, vol. 18, no. 11, pp. 5394–5409, Aug. 2019.
- [10] Q. Liu, J. Wu, P. Xia, S. Zhao, W. Chen, Y. Yang, and L. Hanzo, “Charging unplugged: Will distributed laser charging for mobile wireless power transfer work?” *IEEE Veh. Technol. Mag.*, vol. 11, no. 4, pp. 36–45, Nov. 2016.
- [11] G. J. Linford, E. R. Peressini, W. R. Sooy, and M. L. Spaeth, “Very long lasers,” *Appl. Opt.*, vol. 13, no. 2, pp. 379–390, Feb. 1974.
- [12] J. Lim, T. S. Khwaja, and J. Ha, “Wireless optical power transfer system by spatial wavelength division and distributed laser cavity resonance,” *Opt. Express*, vol. 27, no. 12, pp. A924–A935, June 2019.
- [13] W. Wang, Q. Zhang, H. Lin, M. Liu, X. Liang, and Q. Liu, “Wireless energy transmission channel modeling in resonant beam charging for IoT devices,” *IEEE Internet Things J.*, vol. 6, no. 2, pp. 3976–3986, Jan. 2019.
- [14] M. Xiong, Q. Liu, M. Liu, X. Wang, and H. Deng, “Resonant beam communications with photovoltaic receiver for optical data and power transfer,” *IEEE Trans. Commun.*, May 2020.
- [15] M. Xiong, Q. Liu, G. Wang, G. B. Giannakis, and C. Huang, “Resonant beam communications: Principles and designs,” *IEEE Commun. Mag.*, vol. 57, no. 10, pp. 34–39, Oct. 2019.
- [16] M. Xiong, Q. Liu, G. Wang, G. B. Giannakis, S. Zhang, and C. Huang, “Analytical models for resonant beam communications,” in *International Conference on Wireless Communications and Signal Processing*, Xi’an, China, Oct. 2019, pp. 1–6.
- [17] P. Goetz, W. Rabinovich, S. Binari, and J. Mittereder, “High-performance chirped electrode design for cat’s eye retro-reflector modulators,” *IEEE Photon. Technol. Lett.*, vol. 18, no. 21, pp. 2278–2280, Nov. 2006.

- [18] V. Magni, “Multielement stable resonators containing a variable lens,” *J. Opt. Soc. Am. A*, vol. 4, no. 10, pp. 1962–1969, Oct. 1987.
- [19] H. Kogelnik, “Imaging of optical modes resonators with internal lenses,” *Bell Syst. Tech. J.*, vol. 44, no. 3, pp. 455–494, July 2013.
- [20] P. Baues, “Huygens’ principle in inhomogeneous, isotropic media and a general integral equation applicable to optical resonators,” *Opt. Quantum Electron.*, vol. 1, no. 1, pp. 37–44, Feb. 1969.
- [21] N. Hodgson and H. Weber, *Laser Resonators and Beam Propagation: Fundamentals, Advanced Concepts and Applications 2nd ed.* New York, NY, U.S.: Springer, 2005.
- [22] G. Herziger and H. Weber, “Equivalent optical resonators,” *Appl. Opt.*, vol. 23, no. 10, pp. 1450–1452, May 1984.
- [23] W. Koechner, *Solid-State Laser Engineering, 6th ed.* New York, NY, USA: Springer, 2006.
- [24] I. I. Kim, B. McArthur, and E. J. Korevaar, “Comparison of laser beam propagation at 785 nm and 1550 nm in fog and haze for optical wireless communications,” *Proc. SPIE*, vol. 4214, no. 2, pp. 26–37, Feb. 2001.
- [25] A. E. Siegman, *Lasers*. Mill Valley, CA: University Science Books, 1986.
- [26] V. Petrov, D. Moltchanov, Y. Koucheryavy, and J. M. Jornet, “Capacity and outage of terahertz communications with user micro-mobility and beam misalignment,” *IEEE Trans. Vehi. Technol.*, vol. 69, no. 6, pp. 6822–6827, June 2020.
- [27] D. C. Asoubar, “Simulation of continuous-wave solid-state laser resonators using field tracing and a fully vectorial Fox-Li algorithm,” Ph.D. dissertation, Jena, Germany, 2016.
- [28] U. Simon and F. K. Tittel, “9. nonlinear optical frequency conversion techniques,” *Experimental Methods in the Physical Sciences*, vol. 29, no. 08, pp. 231–278, 1997.
- [29] L. Li, G. Liu, Z. Li, M. Li, H. Li, X. Wang, and C. Wan, “High-efficiency 808-nm InGaAlAsAlGaAs double-quantum-well semiconductor lasers with asymmetric waveguide structures,” *IEEE Photon. Technol. Lett.*, vol. 20, no. 8, pp. 566–568, Mar. 2008.
- [30] A. K. Majumdar, *Advanced Free Space Optics (FSO)*. New York, NY, USA: Springer, 2015.
- [31] F. Xu, M. A. Khalighi, and S. Bourennane, “Impact of different noise sources on the performance of pin- and apd-based fso receivers,” in *Proceedings of the 11th International Conference on Telecommunications*, Graz, Austria, June 2012, pp. 211–218.
- [32] A. J. C. Moreira, T. V. Rui, and A. M. D. O. Duarte, “Optical interference produced by artificial light,” *Wirel. Netw.*, vol. 3, no. 2, pp. 131–140, May 1997.
- [33] C. Quintana, Q. Wang, D. Jakonis, X. Piao, G. Erry, D. Platt, Y. Thueux, A. Gomez, G. Faulkner, and H. Chun, “High speed electro-absorption modulator for long range retroreflective free space optics,” *IEEE Photon. Technol. Lett.*, vol. 29, no. 9, pp. 707–710, May 2017.
- [34] M. S. Demir, F. Miramirkhani, and M. Uysal, “Handover in vlc networks with coordinated multipoint transmission,” in *IEEE International Black Sea Conference on Communications and Networking*, Istanbul, Turkey, June 2017, pp. 1–5.
- [35] F. Zafar, M. Bakaul, and R. Parthiban, “Laser-diode-based visible light communication: Toward gigabit class communication,” *IEEE Commun. Mag.*, vol. 55, no. 2, pp. 144–151, Feb. 2017.
- [36] W. Qin, S. Junique, B. Noharet, S. Almqvist, and J. Y. Andersson, “Multiple quantum well surface normal modulators for free-space optical communication links,” *Proceedings of SPIE the International Society for Optical Engineering*, vol. 6399, pp. 63990A:1–14, Oct. 2006.
- [37] W. S. Rabinovich, G. C. Gilbreath, P. G. Goetz, R. Mahon, D. S. Katzer, K. Ikossi-Anastasiou, S. C. Binari, T. J. Meehan, M. Ferraro, I. Sokolsky, J. A. Vasquez, and M. J. Vilcheck, “InGaAs multiple quantum well modulating retro-reflector for free-space optical communications,” in *Free-Space Laser Communication and Laser Imaging*, vol. 4489, International Society for Optics and Photonics. SPIE, Jan. 2002, pp. 190–201.
- [38] Z. Ghassemlooy, W. Popoola, and S. Rajbhandari, *Optical wireless communications: system and channel modelling with Matlab*. CRC press, 2019.

- [39] J. Piotrowski and A. Rogalski, “Uncooled long-wavelength infrared photon detectors,” pp. 115–131, July 2004.
- [40] L. Summerer and O. Purcell, “Concepts for wireless energy transmission via laser,” in *International Conference on Space Optical Systems & Applications*, Jan. 2009.
- [41] J. E. Hastie, S. Calvez, M. D. Dawson, T. Leinonen, A. Laakso, J. Lyytikinen, and M. Pessa, “High power CW red with linearly polarized TEM<sub>00</sub> output beam,” *Opt. Express*, vol. 13, no. 1, pp. 77–81, Jan. 2005.
- [42] J. R. M. Barr and D. W. Hughes, “Coupled cavity modelocking of a Nd:YAG laser using second-harmonic generation,” *Applied Physics B*, vol. 49, no. 4, pp. 323–325, Oct. 1989.
- [43] A. K. Majumdar, “Free-space laser communication performance in the atmospheric channel,” *Journal of Optical & Fiber Communications Reports*, vol. 2, no. 4, pp. 345–396, Nov. 2005.
- [44] D. V. Mercy, “A review of automatic gain control theory,” *Radio Electron. Eng.*, vol. 51, no. 11.12, pp. 579–590, Nov. 1981.
- [45] J. Zhang, H. Chang, X. Jia, H. Lei, R. Wang, C. Xie, and K. Peng, “Suppression of the intensity noise of a laser-diode-pumped single-frequency ring Nd:YVO<sub>4</sub>-KTP green laser by optoelectronic feedback,” *Opt. Lett.*, vol. 26, no. 10, pp. 695–697, May 2001.
- [46] Y. J. Cheng, P. Mussche, and A. Siegman, “Cavity decay rate and relaxation oscillation frequency in unconventional laser cavities,” *IEEE J. Quantum Electron.*, vol. 31, no. 2, pp. 3391–3398, Feb. 1995.
- [47] M. Piche, P. Lavigne, F. Martin, and P. A. Belanger, “Modes of resonators with internal apertures,” *Appl. Opt.*, vol. 22, no. 13, pp. 1999–2006, July 1983.
- [48] R. G. Wenzel, J. M. Telle, and J. L. Carlsten, “Fresnel diffraction in an optical system containing lenses,” *J. Opt. Soc. Am. A.*, vol. 3, no. 6, pp. 838–842, June 1986.
- [49] S. Cao, S. Tu, Y. Huang, F. Hongying, J. Li, H. Xia, and G. Ren, “Analysis of diffraction loss in laser resonator,” *Laser Technology*, vol. 42, no. 3, pp. 400–403, May 2018.